A complex Queen Charlotte Plate Boundary offshore Haida Gwaii

S. J. Oliva[1,2], M. G. Bostock[2], A. J. Schaeffer[3], E. Nissen[1], R. Merrill[2], A. Hughes[2], S. W. Roecker[4], M. R. Nedimovic[5], E. Roland[6], L. L. Worthington[7], M. A. L. Walton[8], A. Gase[6]

[1]School of Earth and Ocean Sciences, University of Victoria, Victoria, BC, Canada
[2]Department of Earth, Ocean and Atmospheric Sciences, University of British Columbia, Vancouver, BC, Canada
[3]Geological Survey of Canada, Pacific Division, Natural Resources Canada, Sidney, BC, Canada
[4]Earth and Environmental Sciences, Rensselaer Polytechnic Institute, Troy, NY, USA
[5]Department of Earth Sciences, Dalhousie University, Halifax, NS, Canada
[6]Geology Department, Western Washington University, WA, USA
[7]Department of Earth and Planetary Sciences, University of New Mexico, NM, USA
[8]Ocean Sciences Division, US Naval Research Laboratory, Stennis Space Center, MS, USA

Key Points:

- Seismicity offshore Moresby Island is east of previously mapped Queen Charlotte fault and on newly identified fault segments
- Fault segmentation is expressed along strike as breaks in seismicity, changes in vergence, and shifts from single to multiple traces
- Previously undocumented deep seismicity clusters beneath Haida Gwaii are consistent with an underthrusting Pacific plate

Corresponding author: S. J. Oliva, soliva@uvic.ca

Abstract

The Queen Charlotte plate boundary marks a transpressional system between the Pacific and North American plates, extending from offshore Haida Gwaii in Canada into southeastern Alaska. Using continuous seismic waveforms from temporary and permanent seismic networks from 1998–2020, we produced a comprehensive catalog of ∼50,000 earthquakes across the region near Haida Gwaii. We used an automated processing technique of auto-regressive phase detection and onset estimation to obtain the initial seismic catalog, integrated existing catalogs, inverted for 3D velocity structure using data from the most well constrained period, and relocated the entire catalog using the new 3D velocity model. We investigate the seismically active sections of the transcurrent Queen Charlotte fault (QCF), noting that little seismicity locates directly along the bathymetrically defined QCF trace. Instead, the seismicity illuminates a complex system of multiple segmented structures, featuring variable geometries along strike. Clustered shallow seismicity could indicate active shallow faults within the highly deformed Queen Charlotte terrace. Few aftershocks appear on the thrust plane of the 2012 M_w 7.8 Haida Gwaii earthquake except near its inferred intersection with the QCF between 15 and 20 km depths, suggesting elevated residual stress. Deep (up to ∼20 km) crustal seismicity below central Haida Gwaii aligned parallel to the strike of the thrust plane may manifest the landward underthrusting of the Pacific plate. We also explore the possibility of coseismic strike-slip rupture on the QCF during the 2012 earthquake. Our results provide insights into postseismic strain accommodation and partitioning across this complex oblique transpressive system.

Plain Language Summary

We sought to better understand the complex tectonics offshore Haida Gwaii in western Canada where the Pacific and North American plates slide past one another obliquely, by compiling and analyzing the most comprehensive earthquake catalog in the area from 1998–2020. We identify and interpret various earthquake clusters that illuminate (1) a highly deformed terrace of elevated seafloor west of Haida Gwaii, (2) a complex and segmented fault system adjacent to the previously-mapped surface trace of the main Queen Charlotte strike-slip fault, and (3) the inferred fault intersection at depth between the Queen Charlotte fault (which hosted the 1949 magnitude 8.1 earthquake) and the Haida Gwaii thrust (which hosted the 2012 magnitude 7.8 earthquake). We present the most

detailed report to date of the earthquake-producing structures in the region, including previously unidentified and highly segmented faults. We also speculate that the 2012 magnitude 7.8 earthquake on the shallowly dipping Haida Gwaii thrust fault may have also involved some motion on the subvertical Queen Charlotte fault. These results contribute to better constraints on the tectonics and hazards in the region.

1 Introduction

Four of Canada's largest instrumentally recorded earthquakes (with magnitudes $\geq$7) have occurred along the Queen Charlotte Plate Boundary (QCPB), including the 1949 M_S 8.1 earthquake (Rogers, 1983) and the 2012 M_w 7.8 Haida Gwaii earthquake (Cassidy et al., 2014; Lay et al., 2013) (Fig. 1). The QCPB is a major transform plate boundary between the oceanic Pacific and continental North American plates that extends from offshore Haida Gwaii to southeastern Alaska. The main plate boundary fault is the 850 km-long right-lateral Queen Charlotte Fault (QCF), which has a slip-rate of 53 mm/yr (Brothers et al., 2020; DeMets et al., 2010; DeMets & Merkouriev, 2016). This offshore fault merges northward into the onshore right-lateral Fairweather fault. To the south, it links to the nominal Queen Charlotte triple junction of the Explorer, Pacific, and North American plates, through its overlap with the northernmost extent of the right-lateral Revere-Dellwood fault near 52°N (Riddihough et al., 1980; Rohr, 2015) (Fig. 1). In this study we focus on the southern QCPB near Haida Gwaii whose two main islands are Graham Island in the north (Haida: *X̲aaydag̲a Gwaay.yaay linag̲waay in X̲ayda Kil*) and Moresby Island in the south (Haida: *T'aaxwii X̲aaydag̲a Gwaay.yaay linag̲waay*) (Fig. 2).

Along the southern QCPB, obliquity in Pacific-North American plate motions with respect to mapped fault geometries introduces a component of shortening (Fig. 1). The degree of obliquity is debated with estimates of plate motion vectors varying between 5° to 20° clockwise from the QCF strike. Tréhu et al. (2015) reported the angle of oblique convergence to be >15° based on the Mid-Ocean Ridge Velocity (MORVEL) global plate motion model (DeMets et al., 2010). Previously, Rohr et al. (2000) estimated ∼26° of plate motion obliquity to the QCF strike, but later revised their QCF trace to 20° of obliquity (Rohr, 2015). An updated global plate reconstruction by DeMets and Merkouriev (2016) produced 21° of obliquity, a departure of 1° from MORVEL (DeMets et al., 2010). Brothers et al. (2020) reconstructed the QCF motion based on tectonic geomorphology and remapped the QCF trace to lie closer to shore between 52–52.4°N compared to Rohr

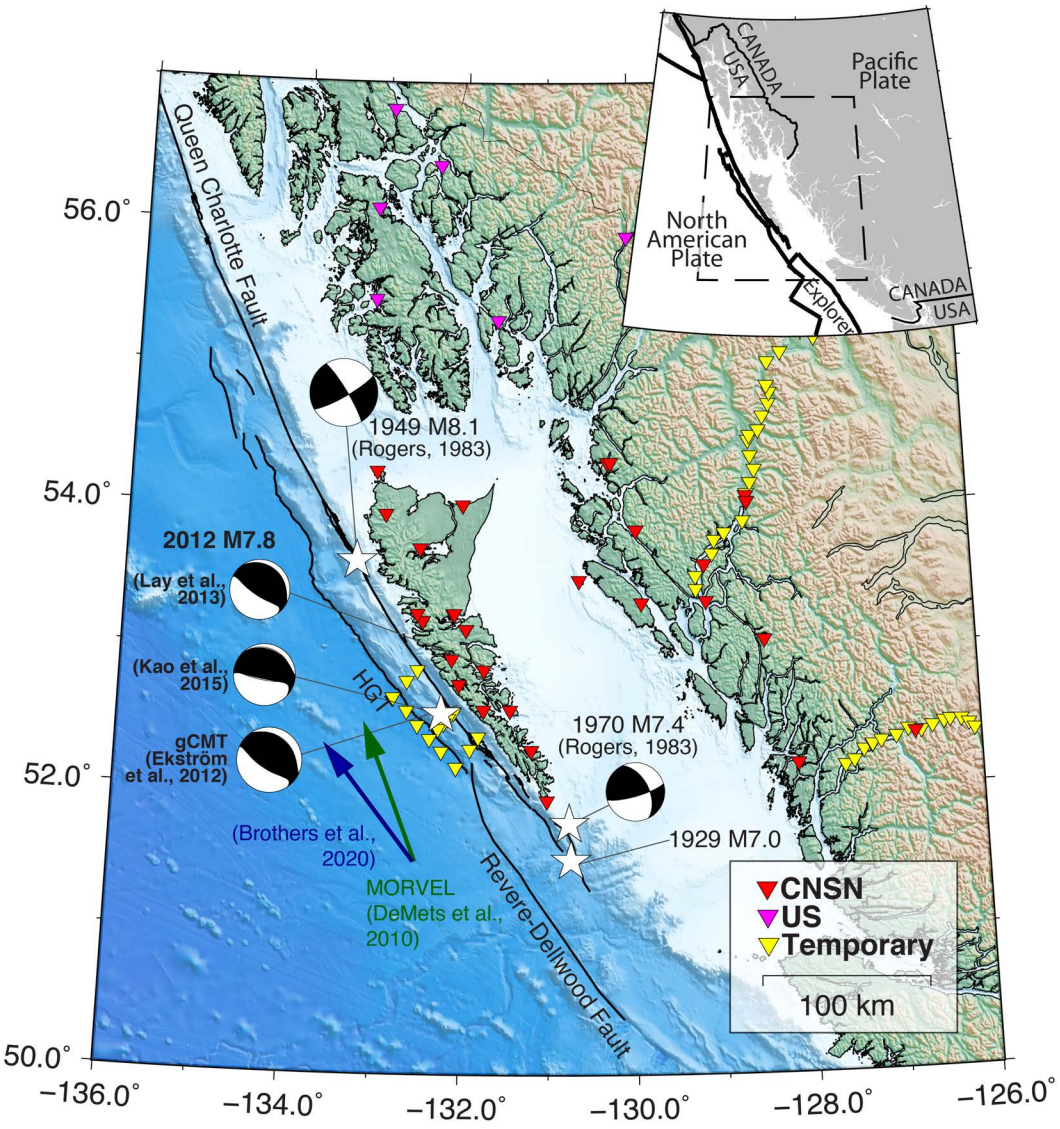

Figure 1. Four M≥7 earthquakes have occurred along the Queen Charlotte Fault during the instrumental period (white stars). Corresponding focal mechanisms for the three most recent events are plotted, including three solutions for the 2012 M_w 7.8 Haida Gwaii earthquake (Kao et al., 2015; Lay et al., 2013; Ekström et al., 2012; Rogers, 1983). Inverted triangles represent seismic stations used in this study where red are part of the Canadian National Seismograph Network (CNSN), magenta are US stations, and yellow are temporary deployments. Mapped fault traces are from Brothers et al. (2020). HGT=Haida Gwaii Thrust fault. Upper right inset shows tectonic context. Green and blue arrows show Pacific plate motion from DeMets et al. (2010) and Brothers et al. (2020), respectively.

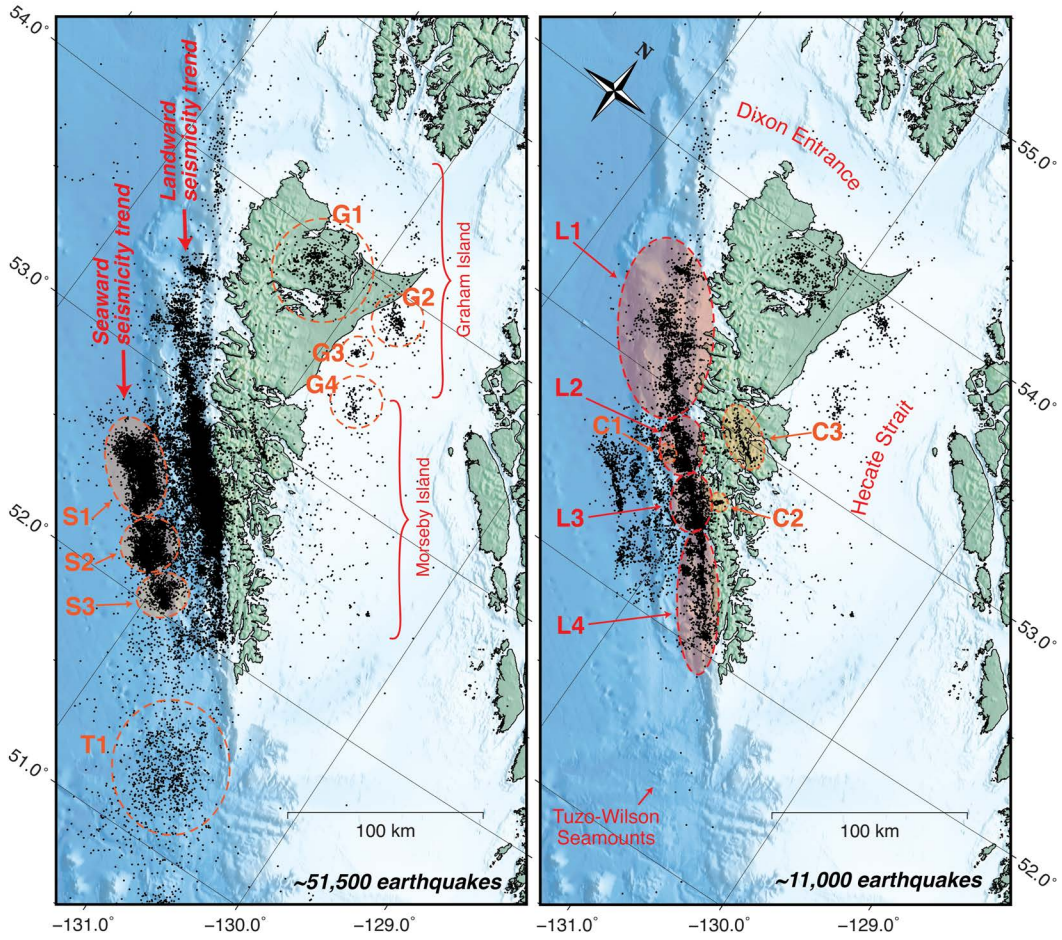

Figure 2. On the full ∼51,500 relocated earthquake catalog (left), we can clearly identify the subparallel seaward and landward seismicity trends. The ∼11,000 subset (right) better shows the seismicity patterns within the landward seismicity trend, labeled as clusters L1 through L4. Clusters C1–C3 are secondary seismicity patterns of interest. Graham (Haida: *X̲aaydag̲a Gwaay.yaay linag̲waay in X̲ayda Kil*) and Moresby (Haida: *T'aaxwii X̲aaydag̲a Gwaay.yaay linag̲waay*) Islands are the two main islands of Haida Gwaii. Hecate Strait separates Haida Gwaii from the mainland and Dixon Entrance serves as the US-Canada border north of Haida Gwaii. Please refer to Fig. 3 for interpreted locations of the principal QCF trace which are not plotted here so as not to obscure seismicity or bathymetric detail.

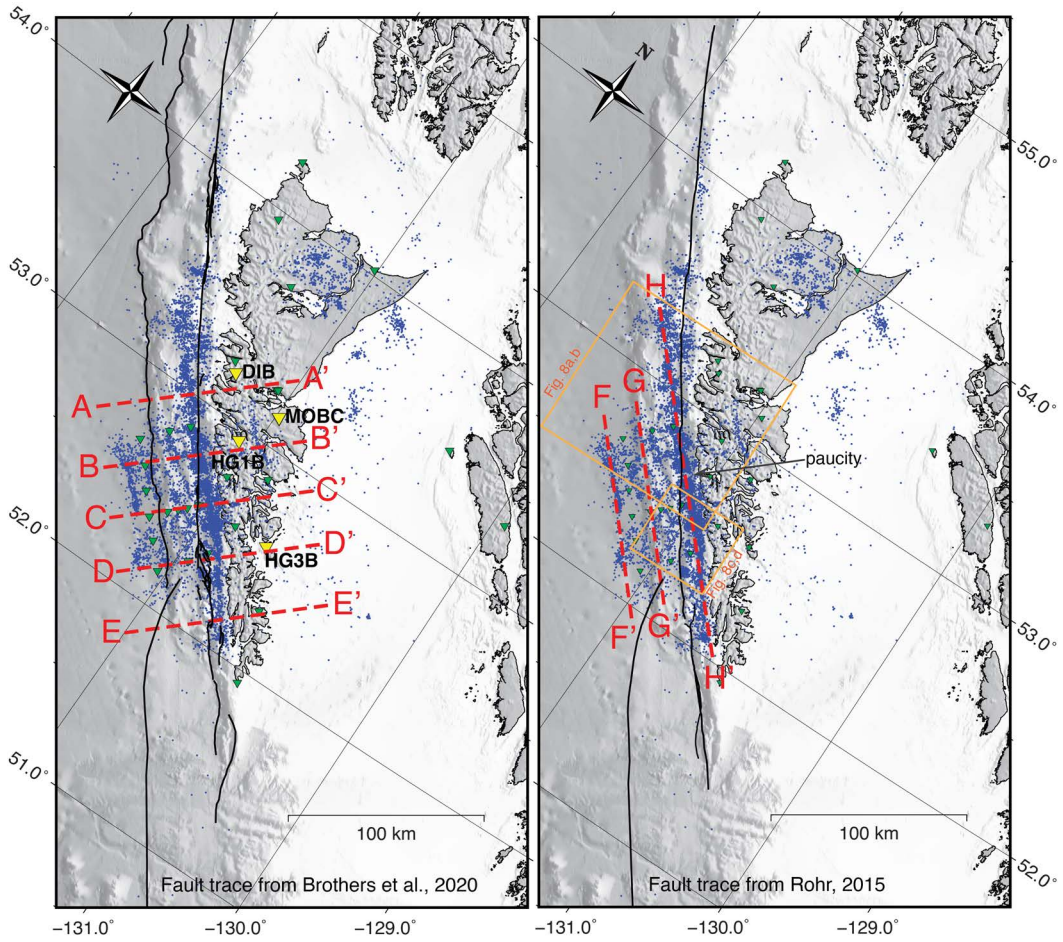

Figure 3. Map of the ∼11,000 earthquake subset (blue) with the across-fault (left) and along-strike (right) transects shown in Figs. 5 and 6, respectively. Receiver functions plotted on Fig. 5 are from stations DIB, MOBC, HG1B, and HG3B, labeled yellow on the left. Stations are green triangles. The mapped QCF traces of Brothers et al. (2020) and Rohr (2015) are shown in the left and right panels, respectively. Orange boxes are locations of Fig. 8.

(2015) (Fig. 3). On the basis of bathymetric signature and a near small-circle trajectory on more northerly portions of the QCF, Brothers et al. (2020) further argued that global plate motion models significantly overestimate convergence along southern Haida Gwaii and that true obliquity is only 5.6°.

In addition to the degree of plate-motion obliquity along Haida Gwaii, debate has also centered on whether convergence is accommodated by underthrusting of the Pacific plate beneath the North American plate (DeMets & Merkouriev, 2016; Hyndman, 2015; Wang et al., 2015) or by internal deformation of the Pacific and North America plates,

involving lithospheric thickening and shortening (Brothers et al., 2020; Rohr et al., 2000). Receiver function studies provide evidence for a 10–17 km-thick low velocity zone dipping 15–30° and extending at least 50 km landward of the QCF beneath Haida Gwaii, interpreted as the top of the underthrusting Pacific plate (Bustin et al., 2007; Gosselin et al., 2015; Smith et al., 2003). Seaward and subparallel to the QCF, the 30 km-wide submarine Queen Charlotte terrace (QCT), composed of faulted and folded sediments and possibly oceanic crust (Riedel et al., 2021; Rohr et al., 2000; Tréhu et al., 2015), has been likened to an accretionary prism, thus pointing to possible subduction initiation (Hyndman, 2015). Within an incipient subduction configuration, the terrace would define a forearc sliver, a feature observed in various other oblique convergent settings around the world (Cassidy et al., 2014; Jarrard, 1986). In this study, we use the terminology "Haida Gwaii thrust fault (HGT)" (Hyndman, 2015) to refer to the fault or fault system beneath the terrace that hosted the 2012 M_w 7.8 thrust event (e.g., Lay et al., 2013; Nykolaishen et al., 2015)—the downdip extent of which remains debated. While Cassidy et al. (2014) have taken the 2012 earthquake as the strongest evidence for an underthrusting oceanic plate, the lower obliquity estimates of Brothers et al. (2020) led the latter to deem subduction unlikely. In the no-slab model, the terrace would represent oceanic crust deformed and thickened from compression (Dehler & Clowes, 1988; Rohr et al., 2000) with the QCF identified as the backstop of deformation concentrated along the edge of a hot and weak oceanic plate (Brothers et al., 2020).

The M_w 7.8 earthquake occurred on October 28, 2012 (October 27, local time) along the QCPB offshore Moresby Island (Fig. 2). The earthquake produced a local tsunami and had a predominantly thrust mechanism, with the preferred fault plane dipping shallowly NNE and striking 311° (Kao et al., 2015), 317° (Lay et al., 2013), or 318° (the global Centroid Moment Tensor or gCMT, Ekström et al., 2012) (Fig. 1). There were very few thrust aftershocks (Kao et al., 2015; Lay et al., 2013), and most of the larger aftershocks were normal-faulting events located west of the QCT, interpreted as evidence for bending stresses on the Pacific plate (Kao et al., 2015) and consistent with modelled Coulomb stress changes (Lay et al., 2013). Whereas back-projected high-frequency seismic radiation might suggest energy release farther downdip beneath Moresby Island (Lay et al., 2013), Global Navigation Satellite System (GNSS) coseismic displacements suggest that rupture probably does not extend farther landward from the coast (Nykolaishen et al., 2015). However, the GNSS-derived slip model resolution is limited during the 2012 main-

shock as there was only one continuous GNSS site in operation, located 80 km to the north-northeast. GNSS-based models of postseismic deformation reveal up to 0.3 m of thrust afterslip downdip of the coseismic rupture within 7 years of the mainshock (Tian et al., 2021), along with between 1.5 and 9.0 cm of right-lateral afterslip on the vertical QCF in the first year (Guns et al., 2021). These models are consistent with repeating earthquakes which suggest short-lived postseismic motion on the QCF (∼2 months) and longer on the HGT (at least 3 years) (Hayward & Bostock, 2017).

The QCPB appears to reside primarily if not entirely offshore, resulting in generally poor azimuthal seismic coverage since regional land stations are all located east of the plate boundary. Fortunately in December 2012, in response to the M_w 7.8 earthquake, the Geological Survey of Canada deployed 14 ocean-bottom seismometers (OBS) offshore Haida Gwaii to record aftershocks (Fig. 1) (Riedel et al., 2021), providing about two weeks of improved data coverage to constrain the plate boundary and the offshore seismicity. Moreover, an additional 7 short-period land stations were deployed in the first week of November 2012; one was only operational for a month (MOBC2), three recorded data until May 2013 (HGPB/HGSB, TSUB, STJA), and the other three had broadband instruments swapped in after the first week (Gosselin et al., 2015). Of the broadband stations, HG3B continued running until 2014, HG1B remains in operation to the current date, and HG4B was reoccupied as JEDB and is active to this day. Capitalizing on these ten years of improved seismic instrumentation, as well as seismic data from twenty years prior, our study aims to characterize the seismicity along the southern QCPB offshore Haida Gwaii in space and time. We use the new earthquake catalog to investigate the configuration of and strain accommodation across the plate margin, including underthrusting along the HGT, the transform QCF, and the potential role of the QCT as a "forearc" sliver.

2 Data and Methods

To augment the existing Geological Survey of Canada earthquake catalog, we adopted a hybrid method of autoregressive phase detection and onset estimation, using `REST` software (Regressive ESTimator) written and maintained by S. W. Roecker, based on detection and onset estimation described by Kushnir et al. (1990), the travel time computation algorithm of Roecker et al. (2006), and the iterative refinement of onset estima-

tion described by Rawles and Thurber (2015). The software is discussed in detail in Comte et al. (2019) and Lanza et al. (2019).

To create our new catalog, we used all available seismic waveform data from 1998 to 2020 for the region between longitudes 136°W and 126°W and latitudes 50°N and 57°N, including the two transects of the Batholiths project (2005-2006) across the Coast Mountains (Calkins et al., 2010) and the Geological Survey of Canada's OBS deployment in 2012 (Riedel et al., 2021). Our automated catalog included 47,628 events with at least 4 paired P and S picks. Within the same time period and region, the Canadian National Seismographic Network (CNSN) reported 14,716 earthquakes. We also included an additional 643 events registered by the CNSN between 1992 to 1998, as well as the Alaska Network (AK) catalog which reported 355 earthquakes in the region over the period 1998–2020. We combined the three catalogs (REST, CNSN, AK), merging events with origin times within 5 s and located within 0.5° latitude and longitude. Automated REST picks were overwritten with CNSN and AK event picks (which are generally screened by analysts), when available for the same event.

The combined catalog with merged picks (53,933 events with at least 4 paired P and S picks) was relocated with `Hypoinverse v.1.4` using the program's multimodel feature. An oceanic velocity model based on a 1983 seismic refraction project west of Haida Gwaii in the Pacific (Dehler & Clowes, 1988) was assigned west of the QCF trace of Rohr (2015), and a continental model based on a 1988 seismic refraction-reflection survey east of Haida Gwaii in the Hecate Strait (Line 6 Spence & Asudeh, 1993) was assigned to the east. We assumed an initial Vp/Vs ratio of 1.76, determined from a Wadati plot of the initial catalog. Given the large number of earthquakes, we sought to better define the associated velocity structure using a small but densely sampled subset of the catalog before relocating the remaining events.

The two weeks with continuous OBS data in December 2012—which, in combination with high aftershock rates, produced the best multi-station coverage of the region—were used to build the 3D velocity model. First we constructed a starting 3D velocity model from the aforementioned 1D oceanic and continental velocity models (Dehler & Clowes, 1988; Spence & Asudeh, 1993), stitched together and smoothed over 30 km across the QCF trace (Rohr, 2015). The model domain is 300 km × 400 km × 200 km, centered at 53°N 132.6°W, rotated 35° counterclockwise, with a nodal spacing of 5 km along

the horizontal and 3 km along the vertical. We performed `Hypoinverse` and `hypoDD` (Waldhauser & Ellsworth, 2000) double-difference relocations separately for the oceanic and the continental sides, then used those relocations as input to the tomographic inversion. The "seaward seismicity trend" (1,028 events) was relocated using a 1D velocity model of the terrace (Dehler & Clowes, 1988) and OBS stations only, such that most wavepaths were beneath the terrace and/or the adjacent Pacific plate (Fig. 2). Similarly, the "landward seismicity trend" (1,680 events) was relocated using a 1D velocity model of the Haida Gwaii islands (Spence & Asudeh, 1993) and land stations only. We used the double-difference seismic tomography code `tomoDD10` (Zhang, 2003; Zhang & Thurber, 2003) to invert for velocity structure only, keeping the earthquake hypocenters constant. In both `hypoDD` and `tomoDD10` inversions, we employed both catalog differential times (`ph2dt`, Waldhauser & Ellsworth, 2000) and cross-correlation differential times (Bostock et al., 2022).

The two weeks of data used in the previous step are dominated by seismicity associated with the aftermath of the 2012 M_w 7.8 event. To expand the 3D velocity model into adjacent regions, we chose a subset of the full `Hypoinverse` earthquake catalog, ensuring good spatial spread of seismicity. We selected earthquakes with root mean squared traveltime residuals less than 1 s and location errors less than 5 km, taking only up to 100 earthquakes with the most phase picks across a $0.1^\circ \times 0.1^\circ$ grid. We also included all earthquakes constrained by OBS, swapping in their `hypoDD` relocations. The resulting catalog of the ∼11,000 best-constrained earthquakes were then used to jointly invert for 3D velocity structure and solve for earthquake hypocenters using `tomoDD10` and incorporating the output 3D velocity model from the previous step as the starting model. The `tomoDD10` inversion was constrained with a total of 838,771 cross-correlation P- and S-differential times, and 5,532,295 catalog P- and S-differential times. Finally, we relocated the remaining ∼42,000 earthquakes using the resulting 3D P- and S-wave velocity models. The final earthquake catalog has 51,562 earthquakes (see Supplementary Materials).

The primary focus of this study is the characterization and interpretation of seismicity in the region, and hence the velocity inversion was conducted primarily to improve the earthquake locations. Given the small number of stations operating over most of the period and the resulting limited resolution, we refrain from interpreting details in the velocity structure beyond noting that they are generally consistent with previous mod-

els (Dehler & Clowes, 1988; Spence & Asudeh, 1993). We present Vp, Vs and Vp/Vs cross sections in the Supplementary Materials.

3 Results

The full catalog clearly delineates two prominent near-parallel seismicity trends (Fig. 2), both oriented about 8° counterclockwise from the previously mapped QCF surface trace by Rohr (2015) and Brothers et al. (2020) (Fig. 3). The "landward seismicity trend" coincides with the QCF trace near 52.8°N but deviates along a trajectory that more closely approaches the coast as one proceeds south. The "seaward seismicity trend" resides in the Pacific plate, parallel to and immediately west of the bathymetric trough that borders the terrace. Because the dense seismicity (and greater average location uncertainty) of the full catalog obscures spatial patterns, especially within the landward seismicity trend, we will focus on the ∼11,000 subset of best resolved earthquakes for which details in the seismicity patterns are clearer (Fig. 2b). In the following subsections, we will describe the various earthquake clusters of interest, west to east, north to south. We also consider the temporal dependence of seismicity over three separate intervals: before the 2012 M_w 7.8 event (Fig. 4a), during the aftershock period (Fig. 4b), and from 2016 onwards when the seismicity appears to have leveled off (Fig. 4c,d).

3.1 Seaward Seismicity Trend

The seaward seismicity trend is strongly represented during the aftershock period, with practically no detections prior to 2012 and much reduced levels from 2016 onwards (Fig. 4). Despite the improved seismic network coverage following the 2012 M_w 7.8 earthquake, the lack of seismic activity prior to 2012 is likely robust. The persistence of modestly elevated seismicity levels from 2016 onward may indicate that the activity here has not yet returned to background levels. Earthquakes here are shallower than 10 km (Fig. 5), suggesting that they reside primarily within Pacific oceanic crust. Kao et al. (2015) demonstrate that the largest aftershocks have mostly normal mechanisms, consistent with an origin related to bending of the oceanic plate. The trend can be divided into three clusters (S1, S2, S3) (Fig. 2a), consistent with Farahbod and Kao (2015) who studied 1,229 aftershocks from the first week following the M_w 7.8 event. The southern cluster (S3) is located around the northern terminus of the Revere-Dellwood fault (RDF) as defined by Rohr (2015) (Fig. 4a). The northern limit of the seaward trend reaches ∼52.7°N, di-

rectly updip from the northernmost (∼52.85°N) end of the pronounced, deep (∼16 km) seismicity of the landward trend (see Fig. 2).

3.2 Landward Seismicity Trend

3.2.1 Offshore Graham Island (Cluster L1)

West of Graham Island, 53.0–53.5°N, seismicity along the QCF flips from predominantly west of the mapped QCF surface trace (Brothers et al., 2020; Rohr et al., 2000), to beneath the trace, and then back to the west, (cluster L1, Figs. 2,4). To the north of 53.5°N, less seismicity is detected (Fig. 6). Ristau et al. (2007) reported only strike-slip moment tensors north of 53°N, whereas they mapped mostly thrust mechanisms to the south. Moreover, the trend of the QCF trace bends clockwise north of 53.2°N, becoming nearly parallel to the plate motion vector and consistent with diminished convergence to the north (Rohr et al., 2000; Tréhu et al., 2015). Thus, ∼53.0–53.5°N appears to define the northern limit of the QCPB transpressive segment, consistent also with the northern extent of the high bathymetric profile of the Queen Charlotte terrace.

3.2.2 Offshore Moresby Island (Clusters L2, L3, L4)

The landward seismicity trend is densest and deepest west of Moresby Island, south of 52.85°N (Fig. 2). Following the landward seismicity trend ∼80 km along-strike from northwest to southeast, there is some lateral segmentation and a slight increase in maximum depth of seismicity from ∼16 to 20 km (H-H', Fig. 6). In map view, we identify three clusters of note (clusters L2, L3, L4, Fig, 2).

Cluster L2 is a near-vertical structure, underlying the previously mapped QCF surface trace, with a maximum depth of ∼16 km, as evident on the across-QCF transect (B-B', Fig. 5). Clusters L2 and L3 are separated by a paucity of seismicity that is most apparent in the ∼11,000 subset catalog. Along L3 and L4, the landward seismicity trend deviates eastwards from the previously mapped QCF surface trace, and approaching the Haida Gwaii coast to the south. Most evident on the cross-sectional view of L3 (see 'shallow LST' and 'deep LST' in C-C', Fig. 5), we identify two subclusters that overlie one another: a shallow subcluster dipping seaward from the surface to ∼10 km depth, and a deep subcluster dipping landward at ∼8–17 km depths. Seismicity levels decrease southward from L3 to L4. The southward continuation of the shallow and deep subclusters

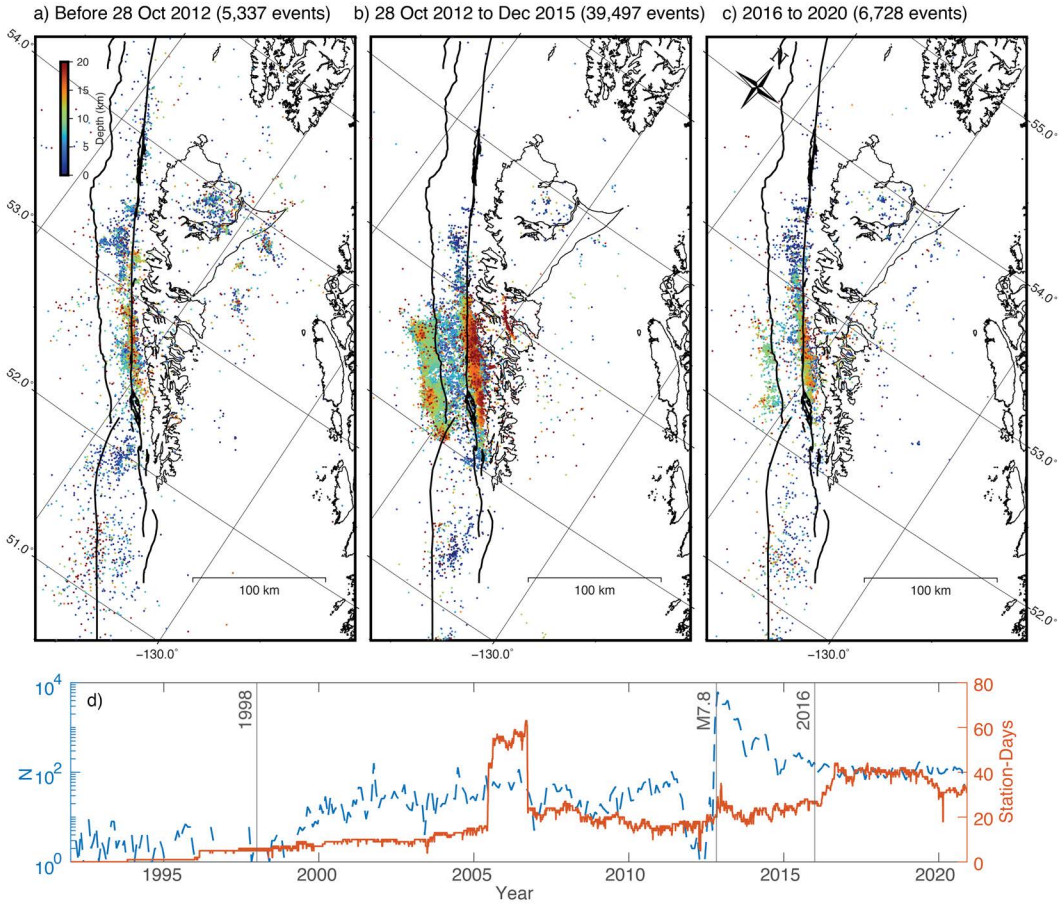

Figure 4. Full seismic catalog split into three time periods: (a) prior to the 2012 M_w 7.8 earthquake, (b) from 28 October 2012 through December 2015, and (c) from 2016 through 2020, colored by depth with deepest plotted on top. The bottom plot (d) shows the station-days over time (solid orange line, right vertical axis) and number of earthquakes over time (dashed blue line, left vertical axis). 1998 signals the start of the automated catalog. M_w 7.8 labels the main-shock along the horizontal time axis and 2016 is when the seismicity seems to have leveled off. Increased station coverage in 2005–2006 is due to inclusion of temporary Batholiths stations (two lines of yellow triangles on the British Columbia mainland in Fig. 1) (Calkins et al., 2010). Mapped fault traces are from Brothers et al. (2020).

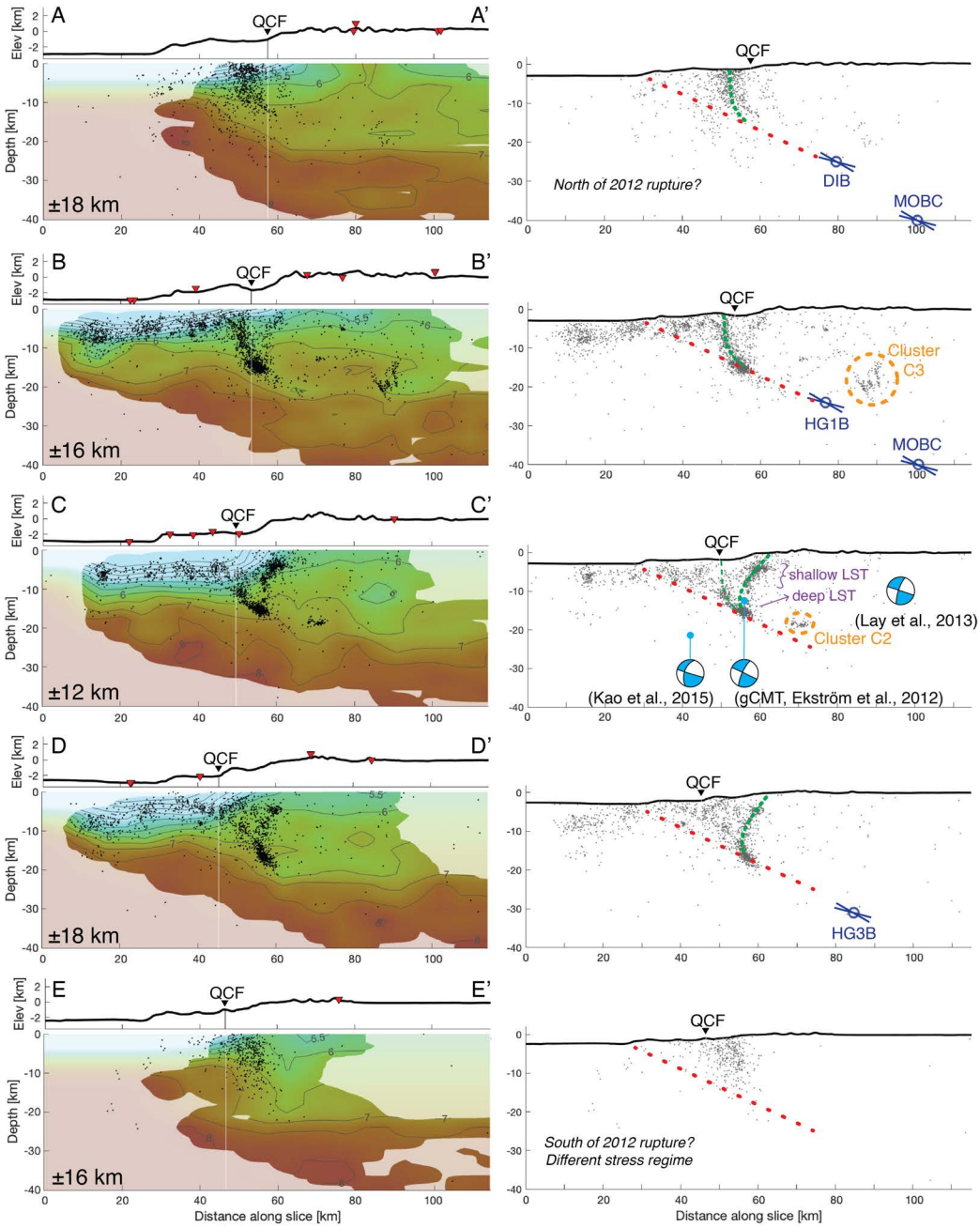

Figure 5. Across-fault cross-sections (see Fig. 3 for map view). Left column shows the Vp sections of the final velocity model (same color scale as Fig. 6). Seismicity projected onto the transects is from the ∼11,000 earthquake catalog and within the distances indicated on the bottom left corner of each panel. Inverted red triangles are stations. Black triangles are where the Queen Charlotte fault (QCF) trace as interpreted by Rohr (2015) intersects with the transects. Right column shows corresponding interpretations of the seismicity. Blue circles are receiver function depths to the top of a low velocity zone, with short blue lines representing 15° and 30° dips (Bustin et al., 2007; Gosselin et al., 2015). For reference purposes, we draw the red dotted lines from the trough to the receiver function depths. Green dotted lines are interpreted faults from the seismicity. Elevation has 2× vertical exaggeration on the left.

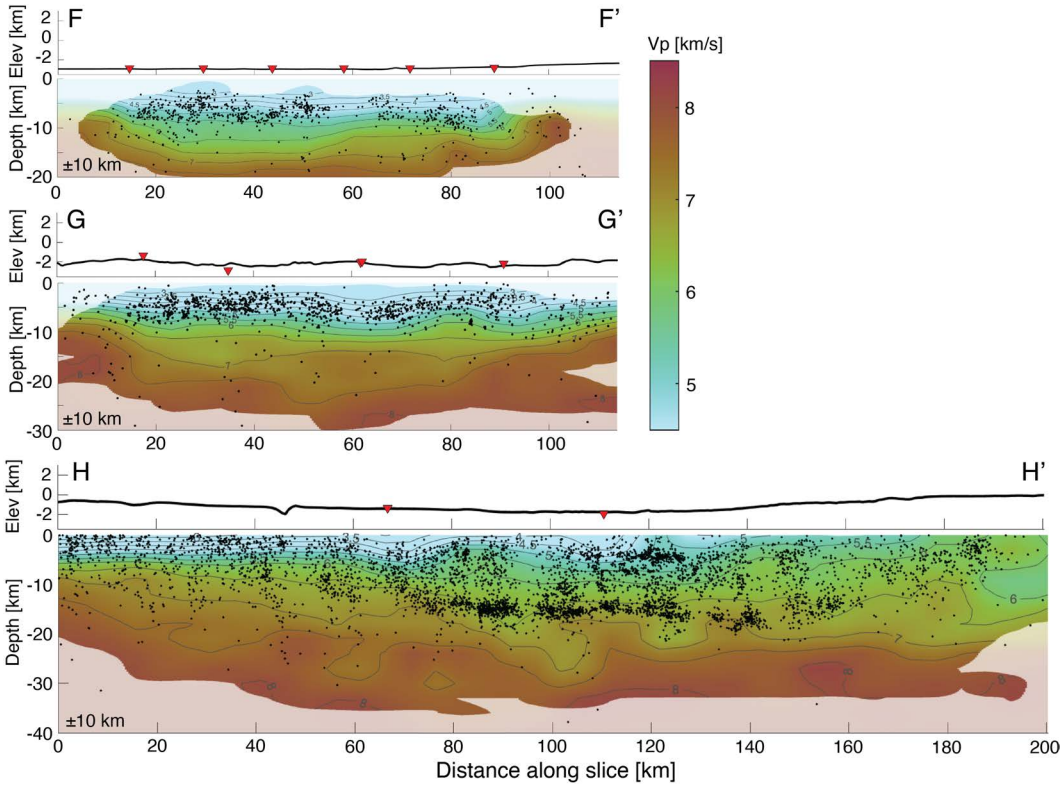

Figure 6. Along-fault cross-sections of the southern Queen Charlotte Plate Boundary: F-F', through the seaward seismicity trend; G-G', through the Queen Charlotte Terrace; and H-H', through the landward seismicity trend (see Fig. 3 for map view). Seismicity from the ∼11,000 earthquake subset, lying within 10 km of each transect, is plotted on the Vp sections of the final velocity model. Inverted red triangles are stations. Elevation has 2× vertical exaggeration.

of L3 persist into L4, with most events located east of the previously mapped QCF surface trace (D-D', Fig. 5). Seismicity extends to ∼20 km depth in L4, such that the landward seismicity trend slightly deepens from north to south (H-H', Fig. 6). Outside of the aftershock period (2012–2016), Clusters L2 and L3 exhibit some activity, but Cluster L4 registers almost no seismicity (Fig. 4).

3.3 Other Earthquake Clusters

Beneath Graham Island and immediately east under the Hecate Strait, there are concentrations of seismicity (clusters G1–G4) that have been previously identified and hypothesized to be related to minor crustal faults by Bird (1999) and Ristau et al. (2007). Near Moresby Island, we identify three clusters of interest, labelled C1, C2, C3 in Fig. 2. Farther south, there is a shallow cluster of earthquakes near the Tuzo-Wilson seamounts (T1 in Fig. 2) which Littel et al. (2023) discuss in detail.

Clusters C1 and C2 represent two small groups of earthquakes that are located just off of the landward seismicity trend (Fig. 2). At ∼52.75°N, Cluster C1 extends west of the QCF trace where most seismicity lies beneath the fault trace, and spreads subvertically from the surface to 12 km depth (Fig. 2). Cluster C2 falls just east of the landward seismicity trend beneath Moresby Island near 52.65°N and concentrates at ∼20 km depth (Fig. 2, C-C' in Figs. 3,5).

Farther landward at the northern end of Moresby Island, we observe a slightly arcuate band of seismicity, subparallel to the two principal seismicity trends (Cluster C3, Fig. 2; B-B' in Figs. 3,5). This feature comprises 168 earthquakes from August–December 2013, with magnitudes ≤∼3 and depths of 15–20 km, that were not reported in the CNSN catalog (Fig. 7). Seismicity here exhibits no evidence for systematic spatiotemporal migration.

4 Discussion

4.1 Constraints on the Haida Gwaii thrust

The Haida Gwaii thrust (HGT) hosted the 2012 M_w 7.8 earthquake but there is debate on whether the underthrusting extends beneath the Haida Gwaii islands. Here we discuss the geometry of the LST and the seismicity clusters beneath Haida Gwaii and how they might provide insights into the extent of underthrusting.

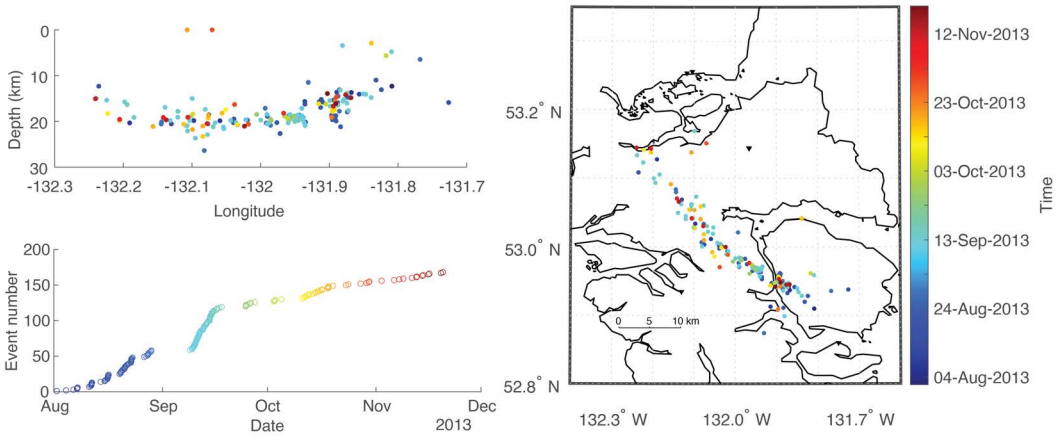

Figure 7. Linear seismicity trend beneath Moresby Island. (Top left) Depth vs. Longitude profile reveals no obvious spatiotemporal migration. (Bottom left) All earthquakes occurred between August and December 2013. (Right) Map view. All events are colored in chronological order from blue to red.

In map view (Fig. 4b), aftershocks appear to delimit the coseismic rupture area (e.g., from Cassidy et al., 2014; Lay et al., 2013), but in cross-section (Fig. 5), there is little indication of the seismicity directly delineating a dipping HGT fault plane. Instead we infer a plausible geometry through consideration of additional constraints. We assume that the surface limit of the HGT coincides with the bathymetric trough, or the deformation front, just west of the terrace, and that the downdip extent is constrained by a well-defined low velocity zone identified by three independent receiver function studies, and interpreted as a proxy for the crust of the underthrust Pacific plate (Bustin et al., 2007; Gosselin et al., 2015; Smith et al., 2003). Receiver function modelling also suggests a slab dip of 15–30° (Fig. 5) (Gosselin et al., 2015), which is consistent with the range of dips (17–25°) from different moment tensor solutions of the 2012 M_w 7.8 earthquake (Ekström et al., 2012; Kao et al., 2015; Lay et al., 2013). For reference purposes, we draw red dotted lines dipping at 25° from the trough at the western edge of the QCT to 25 km depth, and note that landward extrapolation of this line exhibits a close correspondence with the top of the Pacific Plate inferred in the three receiver function studies. Moreover, the maximum depth of landward seismicity (i.e., the base of clusters L2, L3, L4) also aligns neatly with this reference line. The simplest explanation accommodating these and other constraints (the moment tensor fault plane geometry of the 2012 earthquake, its rupture area from standard earthquake scaling, the location of the bathymetric trough,

and receiver function depths and dips) is that the HGT corresponds to the top of the Pacific Plate which underthrusts Haida Gwaii at an average dip near 25°. Furthermore, the deepest seismicity in L2, L3, L4 could be inferred to lie at the downdip terminus of the 2012 rupture and represent stress adjustments near the landward limit of the base of the QCT sliver in its role as a juncture in slip partitioning (e.g., Jarrard, 1986; Wang et al., 2015). If the dipping low-velocity zone documented at a total of 9 stations distributed across Graham and Moresby Islands (Smith et al., 2003; Bustin et al., 2007; Gosselin et al., 2015) has been erroneously attributed to the top of an underthrust Pacific Plate, as would be required by the interpretation of a no-slab model (e.g., Brothers et al., 2020), then the Pacific Plate may extend no farther landward than the deepest extensions of clusters L2, L3, L4. Both interpretations for the landward extent of Pacific plate are consistent with slip modeling of GNSS displacements (Nykolaishen et al., 2015), long period waveform and tsunami modeling (Lay et al., 2013), and downdip location (adjusted relative to centroid) of high frequency body wave radiation from teleseismic back projection (Lay et al., 2013), provided that any Pacific-North America relative plate motion below Haida Gwaii occurs independently and presumably aseismically (Wang et al., 2015).

Clusters C2 and C3 (C-C' and B-B' in Fig. 5) include deep (∼20 km) earthquakes beneath Moresby Island and may afford some constraint on the downdip extent of the HGT. Cluster C3 forms a slightly arcuate band that is subparallel to the two principal seismicity trends, suggesting it is somehow related to the stress regime of the tectonic margin. The continental Moho depths from receiver functions are modelled at ∼18 km just west of C3 and at ∼25 km to the east (HG1B, MOBC, Fig. 3), while the Moho depth estimates nearest to C2 are at ∼18 km (HG1B, HG3B, Fig. 3) (Gosselin et al., 2015). Seismic refraction interpretations are generally consistent with these estimates and suggest that the Moho deepens eastward across Haida Gwaii from 21 to 28 km (Mackie et al., 1989; Spence & Asudeh, 1993). Accordingly, clusters C2 and C3 likely reside within the lowermost crust which must be sufficiently cool to support brittle deformation at depth. Here we consider several additional relevant observations. First, the nearest heat flow measurement is 47 mW/m^2 from a site some 10 km NW of C2 and 20 km SW of C3 (Hyndman et al., 1982). This value is comparable to those measured in south-central Vancouver Island (36–45 mW/m^2; Lewis et al., 1988) where the Juan de Fuca plate is of similar age to the Pacific plate off Haida Gwaii. Moreover, the Wrangellia terrane forms the North

American crustal basement in both locations. Thermal modelling of heat flow observations in southern Vancouver Island (Gao & Wang, 2017) and Haida Gwaii (Wang et al., 2015) incorporating subduction yields similar temperatures near 350°C at 25 km depth. This depth corresponds to the maximum depth of earthquakes in Wrangellia on southern Vancouver Island (Savard et al., 2018). Thus we conclude that the locations and depths of clusters C2 and C3 are consistent with the presence of an underthrust Pacific Plate below Haida Gwaii.

4.2 Constraints on the Queen Charlotte fault system

Previous regional seismicity studies have inferred the QCF to approach the coast southward along Haida Gwaii but are based on more diffuse distributions of seismicity with larger location uncertainty (Bird, 1999; Ristau et al., 2007). Our seismicity relocation generally corroborates this, but also indicates increased complexity southward along Moresby Island. Seismicity appears adjacent to the mapped fault traces in the north (A-A' and B-B' in Fig. 3), then approaches the coast to the south, up to ∼10 km east of the previously mapped QCF surface trace. In particular, we identify a) significant departures from verticality, and b) multiple active strands, which we describe further below.

Acknowledging the poor constraints on the QCF geometry at depth, Wang et al. (2015) have hypothesized that it may dip steeply eastward off Moresby Island, noting that while the focal mechanism of the largest strike-slip earthquake in the region (1949 M_S 8.1) features a near-vertical fault plane, the 1970 M7.4 strike-slip event to the south has a northeast-dipping preferred nodal plane. Moreover, whereas a focal mechanism for the 1929 M7.0 earthquake could not be calculated, a 1 m-high local tsunami was reported which is consistent with some component of thrust (Cassidy et al., 2010; Rogers, 1983). The steep apparent dip evident at the southern end of L1 (A-A', B-B', Fig. 5) is consistent with the preferred fault plane (strike=327°, dip=82°) (Rogers, 1983) of the 1949 M_S 8.1 earthquake to the north which ruptured through this section (Bostwick, 1984; Rogers, 1983).

We observe segmentation and along-strike complexity in the cross-sectional concentrations of seismicity along the landward seismicity trend. Along L2, we observe a transition from primarily seaward vergence in the north to landward vergence in the south

(evident in cross-section view, B-B' and C-C', Fig. 5), accompanied by a paucity in earthquakes along-strike at ∼52.7°N (evident in map view, Figs. 3, 8b). Transects B-B', C-C', and D-D' all display seismicity concentrations at depth. As discussed in section 4.1, this feature is interpreted here as the merger of the QCF with the HGT, and is notably absent along cross-sections A-A' and E-E' that lie outside the 2012 rupture zone. Moreover, some portion of this deep seismicity may represent aftershocks at the downdip limit of the 2012 M_w 7.8 rupture.

Although the location of the previously mapped QCF trace off Graham Island and farther north is clearly demarcated by its bathymetric expression (e.g., Brothers et al., 2020; Rohr, 2015), its definition southward along Moresby Island becomes more complex. The development of the QCT as a highly deformed sliver in response to compression means that there are multiple faults and folds evident on the seafloor that complicate interpretation of the QCF in this region. Indeed, Rohr (2015) and Brothers et al. (2020) mapped the QCF trace off Moresby Island based on seafloor geomorphology and seismic reflection (see Fig. 3) with slightly different trajectories. The location of the QCF trace is also characterized by a narrow, vertical low velocity zone down to about 6 km depth (Dehler & Clowes, 1988; Riedel et al., 2021), but such structures are beyond the resolution of our tomography.

The QCF traces as mapped by Rohr (2015) and Brothers et al. (2020) are identical north of 52.4°N and display deviations only southward of it (around D-D' in Figs. 3, 8d). In our own morphology assessment using available high-resolution multibeam swath bathymetry (Barrie et al., 2013) and SeaMARC II sidescan sonar data (Davis et al., 1987), the deviations begin south of ∼52.6°N (Fig. 8b,d). Figs. 8a,b provide an expanded view of the bathymetry in the northern region and its relation to seismicity. Immediately south of the left (compressional) step-over at 53.2°N, seismicity is dominantly shallow (<5 km) and lies seaward of the QCF trace indicating that it is focused within the sediments of the terrace. In particular, there appears to be an association between shallow earthquakes and at least one fold crest that may be rooted by an out-of-sequence thrust fault (see bathymetric profile in Fig. 8g across profile w-w' defined in Fig. 8a), though more data are required to confirm this. As one proceeds southward into the rupture area of the 2012 event (midway between A-A' and B-B'), the average depth of seismicity increases and deep (>14 km) events become more prevalent and organized immediately landward of the principal QCF trace. Shallow seismicity persists seaward below the terrace with one

concentration in alignment with a scarp. This is also evident in cross-sectional view (Fig. 5) where shallow seismicity is seemingly confined to a wedge-shaped block or sliver beneath the terrace, possibly occurring on imbricate faults or flower structures, though further data is needed to precisely identify the structures. Between B-B' and C-C', the paucity in earthquakes along-strike at ∼52.7°N coincides with a discontinuity in our mapped faults, which seems to mark the end of a well-defined single fault trace to the north. To the south-east of C-C' (Figs. 8c,d), a principal QCF surface trace is more difficult to distinguish and we interpret several distributed scarps. The most landward of these scarps skirts the edge of the shelf for 15–20 km as evident in bathymetry both in and between canyons (see Figs 8e,f; profiles x-x', y-y', z-z'). This feature appears to be associated with and could be a host structure to the corresponding section of the landward seismicity trend.

4.3 Reinterpreting postseismic earthquakes

Our new seismicity catalog hints that the QCF played a significant role in the 2012 M_w 7.8 event, since the landward seismicity trend adjacent to the QCF was especially well represented during the aftershock period. In this section we explore the feasibility of slip partitioning onto the QCF coeval with the 2012 earthquake using moment tensor analysis. We present two possible, not necessarily mutually exclusive, endmember interpretations for the aftershocks on the QCF, related to whether or not there was coseismic slip on the QCF.

In the first scenario, these aftershocks could be related to previously undocumented coseismic slip shallower than ∼15 km on the QCF during the 2012 thrust mainshock. At 15–20 km depth, they may define the downdip limit of the 2012 M_w 7.8 rupture, consistent with the distribution of coseismic HGT slip (3–6 m slip contours from Lay et al., 2013), and may also coincide with the source of the coseismic high frequency body wave energy modeled by Lay et al. (2013).

In the second scenario, the landward seismicity trend does not include aftershocks to coseismic slip on the QCF per se, but instead manifests significant aseismic afterslip on the QCF. Nykolaishen et al. (2015) hinted at the possibility of induced aseismic slip on the deeper QCF based on the observed southeasterly postseismic displacements at GNSS stations on the southern half of Moresby Island. Postseismic strike-slip motion, especially at 10–20 km depth, is also supported by Coulomb stress estimates of Hobbs

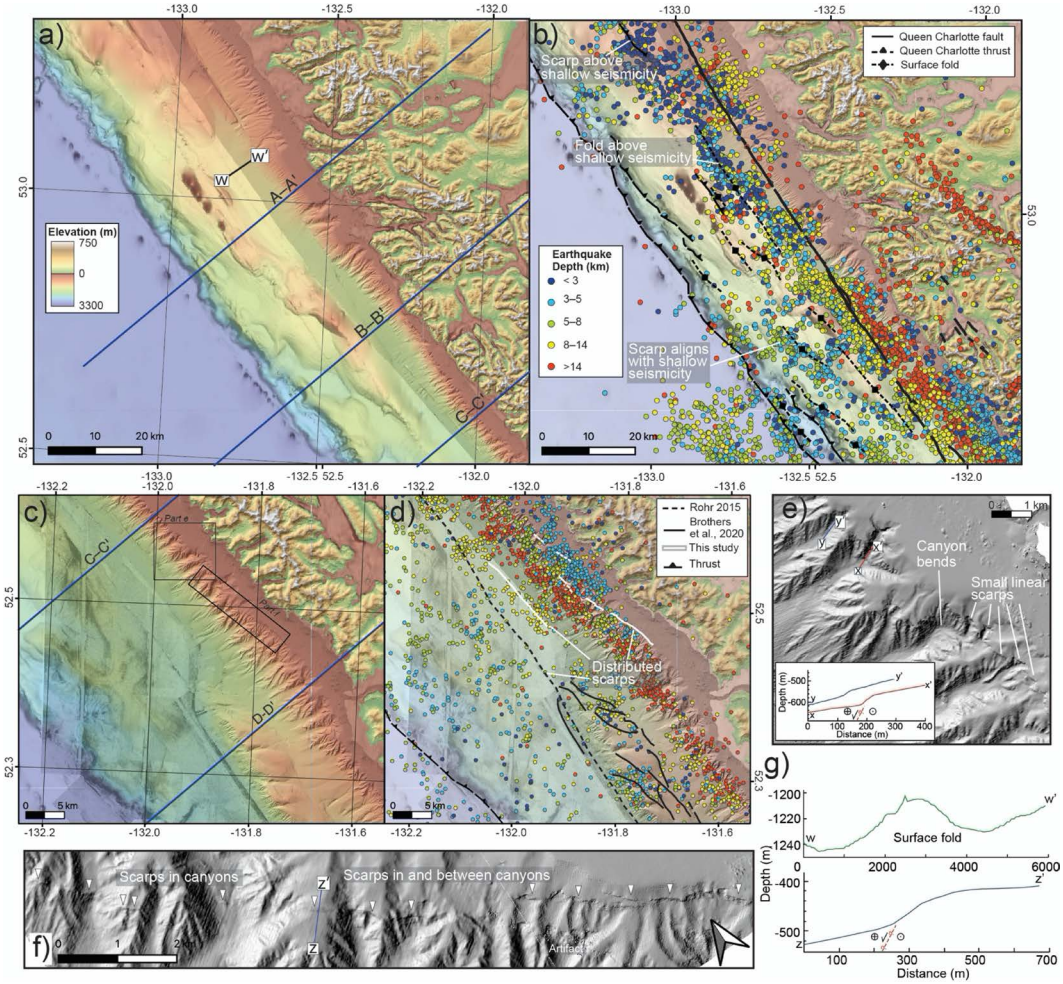

Figure 8. Surface morphology and seismicity. a) Regional Global Multi-Resolution Topography bathymetry (Ryan et al., 2009) showing the morphology of the Queen Charlotte Terrace (QCT) offshore Graham Island, with cross-section lines of Fig. 5 in blue. The slightly darker area immediately offshore shows the limit of high-resolution bathymetry with a grid size of 5 m (Barrie et al., 2013). b) Same map as a) with interpretations from this study and earthquake epicenters colored by depth. Dashed black lines with teeth follow the trough representing the surface trace of the HGT, solid black lines are scarps associated with the Queen Charlotte Fault (QCF: dashed where inferred/uncertain), and dashed black lines with diamonds are the crests of surface folds. c) SeaMARC II sidescan sonar data (Davis et al., 1987) overlain by the high-resolution bathymetry showing the surface morphology offshore Moresby Island. d) Same map as c) with earthquakes colored by depth, mapped strands of the QCF from previous studies, and new strands identified in this study. e) and f) are shaded relief maps from the high-resolution bathymetry, showing scarps in the canyons and inset shows bathymetric profiles across scarps. g) Bathymetric profiles across a subtle surface fold that aligns with shallow seismicity north of section A-A' (top) and across a section of the scarp in part f) (bottom). Topography on Haida Gwaii islands is the 30-m Advanced Spaceborne Thermal Emission and Reflection Radiometer (ASTER) global dataset.

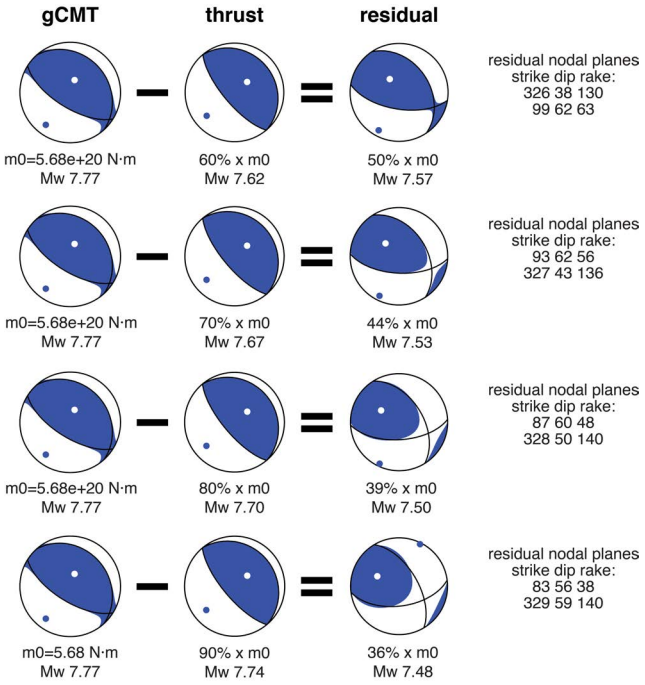

Figure 9. Illustration of theoretical partitioning of the gCMT moment tensor solution into pure thrust and residual events, assuming that the seismic moment of the thrust event is 60–90 % of the composite moment tensor.

et al. (2015) and the activity of repeating earthquakes documented by Hayward and Bostock (2017).

To explore the first scenario, we perform simple tests of whether the seismic moment tensor of the 2012 M_w 7.8 earthquake can be partitioned into a pure thrust event on the HGT and a concurrent strike-slip event on the QCF (Fig. 9). We investigate the non-double-couple gCMT solution of the 2012 mainshock, noting that the non-double-couple nature of a seismic source can arise from fault complexity such as events of differing geometry occurring close together in space and time (e.g., Julian et al., 1998). We assume a pure thrust main earthquake with a strike paralleling both the seaward and landward seismicity trends (strike=320°, dip=18°, rake=90°). Subtracting this theoretical thrust moment tensor at a range of magnitudes, (corresponding to between 60–90% of the total seismic moment of $5.68 \times 10^{(}20)$N-m) from the gCMT solution, we obtain a suite of residual moment tensors. Each of these is observed to have an oblique mechanism with a right-lateral nodal plane close to the strike of the QCF, dipping moderately northeastward at 40–60°. The higher the seismic moment of the thrust event contribu-

tion, the steeper the fault plane dip of the residual moment tensor, with a maximum dip of ∼60° at ∼90% of M_0, consistent at least qualitatively with our inference of a variably dipping QCF. This suggests that, in principle, the slip of the M_w 7.8 earthquake could have been partitioned into near-simultaneous thrust and strike-slip events along the HGT and QCF, respectively. In particular, we note that the location of the QCF surface trace is bathymetrically well defined north of ∼52.6°N (where Rohr (2015), Brothers et al. (2020), and our bathymetric interpretations are fairly in agreement, southwards to between B-B' and C-C'), and that it sits systematically seaward of the deeper (16–20 km) seismicity concentrations profiled in Fig. 5. On the assumption that the principal QCF connects the surface trace with the deep landward seismicity trend, it would dip ∼60° NE on C-C', which is just within the range of dips from the modeling exercise (farther north, the structure would be steeper than suggested by the modeling). One potential caveat is that if coseismic slip did occur along this structure, it would display little evidence for aftershock activity at shallower levels, as is the case on the main thrust plane. However, a scarcity of shallow aftershock seismicity is a common characteristic of large, continental strike-slip sequences, as exemplified by the well-characterized 2000 M_w 6.8 Tottori, Japan, 2003 M_w 6.6 Bam, Iran, 2008 M_w 7.9 Wenchuan, China, 2014 M_w 6.1 South Napa, USA, and 2020 M_w 6.8 Elazığ, Turkey earthquakes (Semmane et al., 2005; Jackson et al., 2006; Tong et al., 2010; Wei et al., 2015; Pousse-Beltran et al., 2020)

GNSS-based modeling of postseismic deformation reveals afterslip on the HGT, downdip of the mainshock, and small right-lateral afterslip on the QCF (Guns et al., 2021; Tian et al., 2021). Repeating earthquakes also indicate thrust and strike-slip afterslip (Hayward & Bostock, 2017), and so both suites of observations are consistent with the second scenario. However, neither approach supplies strong constraints during the coseismic period since there was only one nearby continuous GNSS station running during the earthquake, and small, repeating earthquakes would be obscured by the mainshock and earlier larger aftershocks. Extrapolating the accelerated rates of afterslip from repeating earthquakes in the days and weeks immediately following the mainshock (Hayward & Bostock, 2017) backwards in time supports the possibility of high coseismic slip rates on the QCF during the thrust mainshock, as in the first scenario.

4.4 Tectonic and hazard implications

While the QCPB is considered to comprise a simple and well-defined fault zone in the north along coastal Alaska, our observations together with those of Tréhu et al. (2015) demonstrate that its expression becomes increasingly complex offshore Haida Gwaii. The 1949 M_S 8.1 earthquake ruptured mostly northwestwards (from surface wave directivity and most of the aftershocks occurred to the north) with a smaller component southeastwards (based on five aftershocks southward along the margin, down to 52.0°N) (Bostwick, 1984). This uneven rupture propagation might be due to the increased complexity and fault segmentation to the south, though a preferred directivity arising from a bimaterial contrast across the QCF has also been suggested (Aderhold & Abercrombie, 2015). In light of our results, we may reinterpret the southernmost 1949 aftershocks to be stress adjustments on adjacent faults that did not slip during the mainshock. Instead we speculate that the 1949 M_S 8.1 strike-slip event ruptured through the QCF section dipping steeply landward but no farther southward than ∼52.7°N (between B-B' and C-C' in Fig. 5) where the fault geometry becomes more complex. However, it is important to note, as demonstrated by multi-fault strike-slip earthquakes such as the 2010 M_w 7.2 El Mayor-Cucapah and the 2016 M_w 7.8 Kaikōura earthquakes, that fault segmentation would not necessarily arrest all fault ruptures (e.g., Fletcher et al., 2014; Hamling, 2020).

The lack of HGT seismicity before the 2012 mainshock might imply that the HGT was locked, at least partially, given that repeating earthquake activity suggested some degree of aseismic slip (Hayward & Bostock, 2017). Furthermore, the lack of aftershocks delineating the HGT fault plane suggest a near-total stress drop which has been proposed for megathrust events (e.g., Wetzler et al., 2018). On the other hand, fault locking on the QCF is less straightforward. We have shown that the QCF could have been either locked or slipping during the 2012 mainshock. If the QCF slipped as part of the mainshock, then the sliver would have moved northward in addition to updip as the hanging wall of the HGT, but without GNSS recordings on the terrace this cannot be confirmed. The 2012 M_w 7.8 thrust component likely unclamped the QCF as the sliver moved updip, thus facilitating postseismic motion on the QCF evident in the increase in the number of earthquakes in the landward seismicity trend during the aftershock period.

5 Conclusions

We have employed automatic detection and joint hypocenter-velocity inversion to yield both the largest and highest precision location earthquake catalog for Haida Gwaii assembled to date for the period 1998-2020 that includes the M_w 7.8 October 2012 event. Our relocated earthquakes reveal a number of interesting features:

1. Seismicity is dominated by two parallel strands: a seaward strand just west of the deformation front within the Pacific plate, and a landward strand that runs close to the coast of Moresby island; both of which outline the rupture area of the 2012 M_w 7.8 earthquake. The former has been previously characterized as the response to bending stresses in the Pacific plate. The latter defines a complex system involving multiple structures, the most prominent of which lies offset from the previously mapped QCF surface trace and appears to extend down to seismicity concentrations between 15 and 20 km depth, which plausibly represent stress concentrations at the juncture of slip partitioning between the Pacific and North American plates and the QCT sliver.
2. It is notable that little seismicity locates directly beneath the previously mapped bathymetric QCF trace, a relation that persists north of the 2012 rupture zone to offshore Graham Island. Seismicity in this region appears to be associated with shallower fault structures within the QCT.
3. Significant but less prominent clustered seismicity appears to be associated with shallow crustal faulting and internal deformation within the QCT. This complexity is associated with the uplift and shortening of the terrace sliver in response to highly oblique Pacific-North American plate motion at the southern end of the QCPB.
4. At ∼52.7°N, there is a paucity in earthquakes along-strike, a discontinuity in our mapped fault segments, a change from seaward vergence to landward vergence of the seismicity structure from north to south, and a shift from a single well-identified fault trace to the north to multiple fault segments to the south. These highlight fault complexity south of ∼52.7°N.
5. We note two previously undocumented isolated deep (up to ∼20 km) clusters of seismicity below Haida Gwaii east of the 2012 rupture zone, one of which is approximately linear and extends over ∼40 km and parallels the two main seismic-

ity trends. Their presence is consistent with a significant landward extension of the underthrust Pacific plate below Haida Gwaii.

6. The marked increase and subsequent decrease in microseismicity along the landward trend over the two years immediately following the 2012 event may signify coseismic rupture (M_w 7.5–7.6) along a NE-dipping QCF or, alternatively may represent larger scale postseismic aseismic slip.
7. Modelling the 2012 moment tensor (gCMT) as a combination of pure dip slip along a thrust plane defined by the strike of the seaward and landward seismicity trends and a residual component, allows the possibility of significant (M_w 7.5) coseismic strike-slip motion along a QCF that dips to the NE at ∼40–60°. This scenario is plausible if the QCF surface trace, as defined bathymetrically, joins the landward seismicity concentration at depth (16–20 km). Like the main thrust event, it would imply little or no aftershock activity at shallow levels.

Open Research Section

Raw seismic data are obtained from the Natural Resources Canada (publicly accessible via `ftp://ftp.seismo.nrcan.gc.ca`), and the Incorporated Research Institutions for Seismology (`https://www.iris.edu/`).

Acknowledgments

MGB is funded by an NSERC Discovery Grant (with Department of National Defense Supplement) RGPIN-138004 (with support for SJO). AJS is funded through the Geological Survey of Canada Public Safety Geoscience Program and NSERC Discovery Grant RGPIN-03700-2021 (with support for SJO). EN is funded by NSERC Discovery Grant RGPIN-2023-05278 and Canada Research Chair (with support for SJO). SJO is also supported by the University of Victoria's Hess Postdoctoral Fellowship. We thank Kristin Rohr and Daniel Brothers for providing coordinates for their mapped fault traces. The authors declare no financial conflicts of interest.

References

Aderhold, K., & Abercrombie, R. (2015). Seismic rupture on an oceanic–continental plate boundary: Strike-slip earthquakes along the Queen Charlotte–Fairweather Fault. *Bulletin of the Seismological Society of America*, *105*(2B),

1129–1142.

Barrie, J. V., Conway, K. W., & Harris, P. T. (2013). The Queen Charlotte fault, British Columbia: Seafloor anatomy of a transform fault and its influence on sediment processes. *Geo-Marine Letters*, *33*, 311–318.

Bird, A. L. (1999). *Earthquakes in the Queen Charlotte Islands region: 1982-1996.* (Unpublished doctoral dissertation). University of Victoria.

Bostock, M., Plourde, A., Drolet, D., & Littel, G. (2022). Multichannel alignment of S waves. *Bulletin of the Seismological Society of America*, *112*(1), 133–142.

Bostwick, T. K. (1984). *A re-examination of the August 22, 1949 Queen Charlotte earthquake* (Unpublished doctoral dissertation). University of British Columbia.

Brothers, D. S., Miller, N. C., Barrie, J. V., Haeussler, P. J., Greene, H. G., Andrews, B. D., ... Dartnell, P. (2020). Plate boundary localization, slip-rates and rupture segmentation of the Queen Charlotte Fault based on submarine tectonic geomorphology. *Earth and Planetary Science Letters*, *530*, 115882.

Bustin, A., Hyndman, R., Kao, H., & Cassidy, J. (2007). Evidence for underthrusting beneath the Queen Charlotte Margin, British Columbia, from teleseismic receiver function analysis. *Geophysical Journal International*, *171*(3), 1198–1211.

Calkins, J. A., Zandt, G., Girardi, J., Dueker, K., Gehrels, G. E., & Ducea, M. N. (2010). Characterization of the crust of the Coast Mountains Batholith, British Columbia, from P to S converted seismic waves and petrologic modeling. *Earth and Planetary Science Letters*, *289*(1-2), 145–155.

Cassidy, J. F., Rogers, G. C., & Hyndman, R. D. (2014). An overview of the 28 October 2012 M w 7.7 earthquake in Haida Gwaii, Canada: a tsunamigenic thrust event along a predominantly strike-slip margin. *Pure and Applied Geophysics*, *171*, 3457–3465.

Cassidy, J. F., Rogers, G. C., Lamontagne, M., Halchuk, S., & Adams, J. (2010). Canada's Earthquakes: 'The Good, the Bad, and the Ugly'. *Geoscience Canada*, *37*(1), 1–16.

Comte, D., Farias, M., Roecker, S., & Russo, R. (2019). The nature of the subduction wedge in an erosive margin: Insights from the analysis of aftershocks of the 2015 Mw 8.3 Illapel earthquake beneath the Chilean

Coastal Range. *Earth and Planetary Science Letters*, *520*, 50–62. doi: https://doi.org/10.1016/j.epsl.2019.05.033

Davis, E. E., Currie, R. G., & Sawyer, B. (1987). *Acoustic imagery, southern Queen Charlotte margin.* Geological Survey of Canada. (Preliminary Map 10-1987, 1 sheet) doi: https://doi.org/10.4095/133936

Dehler, S. A., & Clowes, R. M. (1988). The Queen Charlotte Islands refraction project. Part I. The Queen Charlotte Fault Zone. *Canadian Journal of Earth Sciences*, *25*(11), 1857–1870.

DeMets, C., Gordon, R. G., & Argus, D. F. (2010). Geologically current plate motions. *Geophysical journal international*, *181*(1), 1–80.

DeMets, C., & Merkouriev, S. (2016). High-resolution reconstructions of Pacific–North America plate motion: 20 Ma to present. *Geophysical Journal International*, *207*(2), 741–773.

Ekström, G., Nettles, M., & Dziewoński, A. (2012). The global CMT project 2004–2010: Centroid-moment tensors for 13,017 earthquakes. *Physics of the Earth and Planetary Interiors*, *200*, 1–9.

Farahbod, A. M., & Kao, H. (2015). Spatiotemporal distribution of events during the first week of the 2012 Haida Gwaii aftershock sequence. *Bulletin of the Seismological Society of America*, *105*(2B), 1231–1240.

Fletcher, J. M., Teran, O. J., Rockwell, T. K., Oskin, M. E., Hudnut, K. W., Mueller, K. J., ... others (2014). Assembly of a large earthquake from a complex fault system: Surface rupture kinematics of the 4 April 2010 El Mayor–Cucapah (Mexico) Mw 7.2 earthquake. *Geosphere*, *10*(4), 797–827.

Gao, X., & Wang, K. (2017). Rheological separation of the megathrust seismogenic zone and episodic tremor and slip. *Nature*, *543*(7645), 416–419.

Gosselin, J. M., Cassidy, J. F., & Dosso, S. E. (2015). Shear-wave velocity structure in the vicinity of the 2012 M w 7.8 Haida Gwaii earthquake from receiver function inversion. *Bulletin of the Seismological Society of America*, *105*(2B), 1106–1113.

Guns, K., Pollitz, F., Lay, T., & Yue, H. (2021). Exploring GPS observations of postseismic deformation following the 2012 MW7. 8 Haida Gwaii and 2013 MW7. 5 Craig, Alaska earthquakes: Implications for viscoelastic Earth structure. *Journal of Geophysical Research: Solid Earth*, *126*(7), e2021JB021891.

Hamling, I. J. (2020). A review of the 2016 Kaikōura earthquake: insights from the first 3 years. *Journal of the Royal Society of New Zealand*, *50*(2), 226–244.

Hayward, T. W., & Bostock, M. G. (2017). Slip behavior of the queen Charlotte plate boundary before and after the 2012, MW 7.8 Haida Gwaii earthquake: evidence from repeating earthquakes. *Journal of Geophysical Research: Solid Earth*, *122*(11), 8990–9011.

Hobbs, T., Cassidy, J., Dosso, S., & Brillon, C. (2015). Coulomb Stress Changes Following the 2012 M w 7.8 Haida Gwaii, Canada, Earthquake: Implications for Seismic Hazard. *Bulletin of the Seismological Society of America*, *105*(2B), 1253–1264.

Hyndman, R. (2015). Tectonics and structure of the Queen Charlotte fault zone, Haida Gwaii, and large thrust earthquakes. *Bulletin of the Seismological Society of America*, *105*(2B), 1058–1075.

Hyndman, R., Lewis, T., Wright, J., Burgess, M., Chapman, D., & Yamano, M. (1982). Queen Charlotte fault zone: Heat flow measurements. *Canadian Journal of Earth Sciences*, *19*(8), 1657–1669.

Jackson, J., Bouchon, M., Fielding, E., Funning, G., Ghorashi, M., Hatzfeld, D., ... others (2006). Seismotectonic, rupture process, and earthquake-hazard aspects of the 2003 December 26 Bam, Iran, earthquake. *Geophysical Journal International*, *166*(3), 1270–1292.

Jarrard, R. D. (1986). Relations among subduction parameters. *Reviews of Geophysics*, *24*(2), 217–284.

Julian, B. R., Miller, A. D., & Foulger, G. (1998). Non-double-couple earthquakes 1. Theory. *Reviews of Geophysics*, *36*(4), 525–549.

Kao, H., Shan, S.-J., & Farahbod, A. M. (2015). Source characteristics of the 2012 Haida Gwaii earthquake sequence. *Bulletin of the Seismological Society of America*, *105*(2B), 1206–1218.

Kushnir, A., Lapshin, V., Pinsky, V., & Fyen, J. (1990). Statistically optimal event detection using small array data. *Bulletin of the seismological society of america*, *80*(6B), 1934–1950. doi: https://doi.org/10.1785/BSSA08006B1934

Lanza, F., Chamberlain, C., Jacobs, K., Warren-Smith, E., Godfrey, H., Kortink, M., ... others (2019). Crustal fault connectivity of the Mw 7.8 2016 Kaikōura earthquake constrained by aftershock relocations. *Geophysical Research Let-*

ters, *46*(12), 6487–6496. doi: https://doi.org/10.1029/2019GL082780

Lay, T., Ye, L., Kanamori, H., Yamazaki, Y., Cheung, K. F., Kwong, K., & Koper, K. D. (2013). The October 28, 2012 Mw 7.8 Haida Gwaii underthrusting earthquake and tsunami: Slip partitioning along the Queen Charlotte Fault transpressional plate boundary. *Earth and Planetary Science Letters*, *375*, 57–70.

Lewis, T., Bentkowski, W., Davis, E., Hyndman, R., Souther, J., & Wright, J. (1988). Subduction of the Juan de Fuca plate: thermal consequences. *Journal of Geophysical Research: Solid Earth*, *93*(B12), 15207–15225.

Littel, G., Bostock, M., Schaeffer, A., & Roecker, S. (2023). Microplate evolution in the Queen Charlotte triple junction & Explorer region: New insights from microseismicity. *Tectonics*, *42*, e2022TC007494.

Mackie, D., Clowes, R., Dehler, S., Ellis, R., & Morel-À-l'Huissier, P. (1989). The Queen Charlotte Islands refraction project. Part II. Structural model for transition from Pacific plate to North American plate. *Canadian Journal of Earth Sciences*, *26*(9), 1713–1725.

Nykolaishen, L., Dragert, H., Wang, K., James, T. S., & Schmidt, M. (2015). GPS observations of crustal deformation associated with the 2012 M w 7.8 Haida Gwaii earthquake. *Bulletin of the Seismological Society of America*, *105*(2B), 1241–1252.

Pousse-Beltran, L., Nissen, E., Bergman, E. A., Cambaz, M. D., Gaudreau, É., Karasözen, E., & Tan, F. (2020). The 2020 M w 6.8 Elazığ (Turkey) earthquake reveals rupture behavior of the East Anatolian Fault. *Geophysical Research Letters*, *47*(13), e2020GL088136.

Rawles, C., & Thurber, C. (2015). A non-parametric method for automatic determination of P-wave and S-wave arrival times: application to local micro earthquakes. *Geophysical Journal International*, *202*(2), 1164–1179. doi: https://doi.org/10.1093/gji/ggv218

Riddihough, R., Currie, R., & Hyndman, R. (1980). The Dellwood Knolls and their role in triple junction tectonics off northern Vancouver Island. *Canadian Journal of Earth Sciences*, *17*(5), 577–593.

Riedel, M., Yelisetti, S., Papenberg, C., Rohr, K., Côté, M., Spence, G., ... James, T. (2021). Seismic velocity structure of the Queen Charlotte terrace off west-

ern Canada in the region of the 2012 Haida Gwaii Mw 7.8 thrust earthquake. *Geosphere*, *17*(1), 23–38.

Ristau, J., Rogers, G. C., & Cassidy, J. F. (2007). Stress in western Canada from regional moment tensor analysis. *Canadian Journal of Earth Sciences*, *44*(2), 127–148.

Roecker, S., Thurber, C., Roberts, K., & Powell, L. (2006). Refining the image of the San Andreas Fault near Parkfield, California using a finite difference travel time computation technique. *Tectonophysics*, *426*(1-2), 189–205. doi: https://doi.org/10.1016/j.tecto.2006.02.026

Rogers, G. C. (1983). *Seismotectonics of British Columbia* (Unpublished doctoral dissertation). University of British Columbia.

Rohr, K. M. (2015). Plate boundary adjustments of the southernmost Queen Charlotte fault. *Bulletin of the Seismological Society of America*, *105*(2B), 1076–1089.

Rohr, K. M., Scheidhauer, M., & Trehu, A. M. (2000). Transpression between two warm mafic plates: The Queen Charlotte Fault revisited. *Journal of Geophysical Research: Solid Earth*, *105*(B4), 8147–8172.

Ryan, W. B., Carbotte, S. M., Coplan, J. O., O'Hara, S., Melkonian, A., Arko, R., ... others (2009). Global multi-resolution topography synthesis. *Geochemistry, Geophysics, Geosystems*, *10*(3).

Savard, G., Bostock, M. G., & Christensen, N. I. (2018). Seismicity, metamorphism, and fluid evolution across the northern Cascadia fore arc. *Geochemistry, Geophysics, Geosystems*, *19*(6), 1881–1897.

Semmane, F., Cotton, F., & Campillo, M. (2005). The 2000 Tottori earthquake: A shallow earthquake with no surface rupture and slip properties controlled by depth. *Journal of Geophysical Research: Solid Earth*, *110*(B3).

Smith, A., Hyndman, R., Cassidy, J., & Wang, K. (2003). Structure, seismicity, and thermal regime of the Queen Charlotte transform margin. *Journal of Geophysical Research: Solid Earth*, *108*(B11).

Spence, G., & Asudeh, I. (1993). Seismic velocity structure of the Queen Charlotte basin beneath Hecate Strait. *Canadian Journal of Earth Sciences*, *30*(4), 787–805. doi: https://doi.org/10.1139/e93-065

Tian, Z., Freymueller, J. T., & Yang, Z. (2021). Postseismic deformation due to the

2012 M w 7.8 Haida Gwaii and 2013 M w 7.5 Craig earthquakes and its implications for regional rheological structure. *Journal of Geophysical Research: Solid Earth*, *126*(2), e2020JB020197.

Tong, X., Sandwell, D. T., & Fialko, Y. (2010). Coseismic slip model of the 2008 Wenchuan earthquake derived from joint inversion of interferometric synthetic aperture radar, GPS, and field data. *Journal of Geophysical Research: Solid Earth*, *115*(B4).

Tréhu, A. M., Scheidhauer, M., Rohr, K. M., Tikoff, B., Walton, M. A., Gulick, S. P., & Roland, E. C. (2015). An abrupt transition in the mechanical response of the upper crust to transpression along the Queen Charlotte Fault. *Bulletin of the Seismological Society of America*, *105*(2B), 1114–1128.

Waldhauser, F., & Ellsworth, W. L. (2000). A double-difference earthquake location algorithm: Method and application to the northern Hayward fault, California. *Bulletin of the seismological society of America*, *90*(6), 1353–1368. doi: https://doi.org/10.1785/0120000006

Wang, K., He, J., Schulzeck, F., Hyndman, R. D., & Riedel, M. (2015). Thermal condition of the 27 October 2012 M W 7.8 Haida Gwaii subduction earthquake at the obliquely convergent queen charlotte margin. *Bulletin of the Seismological Society of America*, *105*(2B), 1290–1300.

Wei, S., Barbot, S., Graves, R., Lienkaemper, J. J., Wang, T., Hudnut, K., ... Helmberger, D. (2015). The 2014 Mw 6.1 South Napa earthquake: A unilateral rupture with shallow asperity and rapid afterslip. *Seismological Research Letters*, *86*(2A), 344–354.

Wetzler, N., Lay, T., Brodsky, E. E., & Kanamori, H. (2018). Systematic deficiency of aftershocks in areas of high coseismic slip for large subduction zone earthquakes. *Science advances*, *4*(2), eaao3225.

Zhang, H. (2003). *Double-difference seismic tomography method and its applications*. The University of Wisconsin-Madison.

Zhang, H., & Thurber, C. H. (2003). Double-difference tomography: The method and its application to the Hayward fault, California. *Bulletin of the Seismological Society of America*, *93*(5), 1875–1889. doi: https://doi.org/10.1785/0120020190